Journal of
Marine Science and Engineering

MDPI

Article

Comparative Research on Topologies of Contra-Rotating Motors for Underwater Vehicles

Bo Cheng [1,2], Shengzhao Pang [2,*], Huanyu Ou [3], Zeyan Hu [1] and Zhaoyong Mao [2]

1 Institute of Acoustics, Chinese Academy of Sciences, Beijing 100190, China; chengbov@163.com (B.C.); hzy09280928@sohu.com (Z.H.)
2 Unmanned Systems Research Institute, Northwestern Polytechnical University, Xi'an 710072, China; maozhaoyong@nwpu.edu.cn
3 School of Marine Science and Technology, Northwestern Polytechnical University, Xi'an 710072, China; ouhuanyu@mail.nwpu.edu.cn
* Correspondence: shengzhao.pang@nwpu.edu.cn

Abstract: Underwater vehicles have been widely used in marine exploration and development. A contra-rotating propeller (CRP) can improve propulsion efficiency, eliminate the roll moment of the propeller acting on underwater vehicles, and significantly improve the dynamic performance of underwater vehicles. Contra-rotating motors (CRMs) are used to drive CRPs. Topologies of CRMs include an armature rotating contra-rotating motor (ARCRM), double contra-rotating motors (DCRMs), and a double rotor contra-rotating motor (DRCRM). In this paper, the design and optimization of these different topological CRMs were realized with analytical calculations of the magnetic field and electromagnetic performance. The efficiency map and losses analysis of CRMs with different topologies are obtained with the finite element method. In order to achieve suitable CRMs to drive the CRPs of underwater vehicles, three topologies for CRMs will be compared comprehensively from the perspective of structure, weight, size, loss, and efficiency. For low-speed, high-torque CRPs, the ARCRM has been proven to improve efficiency and power density. An ARCRM prototype was developed to verify this solution and its reliability.

Keywords: underwater vehicle; contra-rotating propeller; contra-rotating motor; motor topologies

Citation: Cheng, B.; Pang, S.; Ou, H.; Hu, Z.; Mao, Z. Comparative Research on Topologies of Contra-Rotating Motors for Underwater Vehicles. *J. Mar. Sci. Eng.* **2023**, *11*, 2042. https://doi.org/10.3390/jmse11112042

Academic Editor: Stefano Gaggero

Received: 25 September 2023
Revised: 16 October 2023
Accepted: 20 October 2023
Published: 24 October 2023

1. Introduction

With further exploration and development of the ocean, underwater electric vehicles have attracted more and more attention. In order to reduce resistance during underwater transportation, underwater vehicles can be designed as a streamlined solid of revolution. Propellers are usually used to drive underwater vehicles, but single propellers will have a rolling moment acting on underwater vehicles while providing thrust. For small and high-speed underwater vehicles, rolling may occur during navigation due to low mass and high speed. A contra-rotating propeller (CRP) consists of two coaxial propellers rotating in opposite directions. Since the rear propeller can use the wake of the front propeller, a contra-rotating propeller will have higher propulsion efficiency than a single propeller [1]. Meanwhile, since the torque of the front and rear propellers cancel each other, a CRP can effectively reduce the rolling moment acting on underwater vehicles [2,3]. In order to drive a CRP, a contra-rotating motor (CRM) should have two output ports with opposite rotation directions.

When an underwater vehicle cruises at a low speed, the resistance and thrust required are minor. When an underwater vehicle accelerates, the resistance and thrust required will increase rapidly with the cruising speed [4]. Therefore, higher cruising speed requires the speed and torque of the drive motor to increase rapidly. In order to ensure the dynamic performance and durability of an underwater vehicle, the drive motor should be able to provide sufficient torque and high efficiency in a wide speed range. Due to the strict requirements of underwater vehicles for dynamic performance, the elements of CRMs can be summarized as follows:

(1) Lightweight, high torque density;
(2) High efficiency in a wide speed and torque range;
(3) Strong overload capacity;
(4) Less torque ripple and vibration noise;
(5) Low-frequency maintenance;
(6) Robustness and high reliability.

Since CRMs have more rotating parts and are also expected to have a compact structure and high torque density, permanent magnet (PM) motors are widely used in underwater vehicles. The advantages of PM synchronous motors and PM brushless DC motors make them the preferred candidate for underwater electric transportation. From the perspective of the overall topologies of motors, there are three solutions to drive CRPs: double contra-rotating motors (DCRMs), a double rotor contra-rotating motor, and an armature rotating contra-rotating motor (ARCRM).

(1) DCRMs: two independent motors rotate in opposite directions to drive two propellers of the CRP, respectively.

A contra-rotating axial flux PM synchronous motor was proposed in [5] to drive the CRP of a cylindrical underwater vehicle. It can be seen that a magnetic barrier structure of non-magnetic material is used between the two axial flux magnetic circuits to eliminate the mutual influence of the magnetic fields on both sides.

(2) DRCRM: the motor has an intermediate stator and two PM rotors rotating in opposite directions.

Such a DRCRM may be a radial flux motor with inner and outer rotors and a middle stator [6,7] or an axial flux motor with dual rotors on both sides and a middle stator [8]. In [9–12], F. Zhang and J. Chen et al. have designed a radial flux PM motor with internal and external rotors rotating in opposite directions and processed the prototype for experimental research. The windings on both sides of this prototype are connected in series, so the armature windings on both sides will be crossed so that the phase sequences on both sides are opposite. An axial flux DRCRM was implemented in [13–16], and the windings on both sides were also in series and crossed. The control strategy of this axial flux DRCRM prototype under load variation was discussed in detail. Reference [17] proposed a novel dual-rotor axial flux induction motor for the contra-rotating propulsion systems of underwater vehicles, and this motor has the capability of self-compensating reaction torque for unbalanced loads. Moreover, this type of CRM can also be used in fields such as aircraft propulsion and wind power generation [18,19].

(3) ARCRM: the armature and PM rotors rotate in opposite directions using reactive force. This paper will discuss the motor solution for this topology in detail.

Although multiple topologies for CRMs are mentioned in the references above, there are no papers that conduct comprehensive comparative research on the different topologies of CRMs to investigate which one is more suitable for CRPs of underwater vehicles. This paper aims to explore the magnetic circuit topologies of CRMs for underwater vehicles. First, the analytical design and optimization process of CRMs are presented. Then, the performance and specifications of CRMs with three different topologies will be comprehensively compared and analyzed. Finally, the prototype test of the ARCRM will be carried out.

2. Analytical Design

2.1. Load Characteristics of CRMs

The hydrodynamic performance of a propeller is usually characterized by an advance ratio, thrust coefficient, and torque coefficient [20]. The advance ratio of CRPs is defined by (1):

$$\lambda = \frac{v_t(1 - w_t)}{nD} \tag{1}$$

where v_t is the velocity of underwater vehicles; w_t is the wake coefficient; n is the rotational speed of CRPs, which is also the rotational speed of CRMs; and D is the diameter of the propeller.

The thrust coefficient of CRPs is defined by (2):

$$K_T = \frac{T}{\rho n^2 D^4} \tag{2}$$

where ρ is the density of the seawater, and T is the thrust provided by CRPs, which is equal to the resistance of underwater vehicles.

$$T = C_{x\Omega}\frac{1}{2}\rho {v_t}^2\Omega_t \tag{3}$$

where Ω_t is the characteristic area of underwater vehicles, and $C_{x\Omega}$ is the resistance coefficient of underwater vehicles [21].

The torque coefficient of CRPs is defined by (4):

$$K_Q = \frac{Q}{\rho n^2 D^5} \tag{4}$$

where Q is the input torque of CRPs, equal to the output torque of CRMs.

When the advance ratio is given for a specific CRP, the corresponding thrust coefficient and torque coefficient can be obtained through testing or simulation. When the velocity of the underwater vehicle increases, the rotation speed of the CRP also varies with the velocity. From (1–4), it can be deduced that the input torque of the CRP is proportional to the square of the rotational speed, and the input power of the CRP is proportional to the cube of the rotational speed. The load characteristics of the CRP are shown in Figure 1.

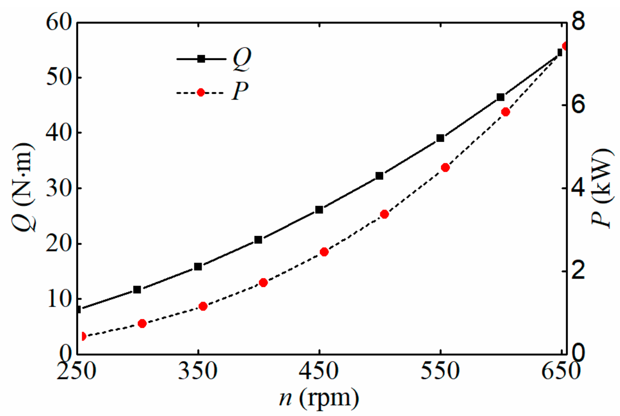

Figure 1. Load characteristics of CRMs.

2.2. Analytical Calculation

The analytical model of the magnetic field generated by PMs is shown in Figure 2, where regions I and III are air, and region II is the PMs. For motors with an internal rotor, $R_0 = R_r$. For motors with an external rotor, $R_s = R_m$. In the coordinate system, by solving the Poisson equation and Laplace equation of the scalar magnetic potential in the PM and air-gap regions, the radial and circumferential components of air-gap flux density in the region I generated by PMs can be derived, as shown in (5) and (6), respectively.

$$B_{rI}(r,\theta,t) = \sum_{n=1,3,5\ldots}^{\infty} K_B(n) f_{Br}(r)\cos[np(\theta-\omega t)] \tag{5}$$

$$B_{cI}(r,\theta,t) = \sum_{n=1,3,5\ldots}^{\infty} K_B(n) f_{Bc}(r)\sin[np(\theta-\omega t)] \tag{6}$$

where,

$$K_B(n) = -\frac{\mu_0}{\mu_r+1}\frac{K_{B(a)}+K_{B(b)}}{K_{B(c)}} \tag{7}$$

$$K_{B(a)} = -\frac{npM_{rn}}{1+np}\left[1-\left(\frac{R_r}{R_m}\right)^{np+1}\right]\left[1-\frac{\mu_r-1}{\mu_r+1}\left(\frac{R_0}{R_r}\right)^{2np}\right] \tag{8}$$

$$K_{B(b)} = \frac{npM_{rn}}{1-np}\left[\left(\frac{R_r}{R_m}\right)^{2np}-\left(\frac{R_r}{R_m}\right)^{np+1}\right]\left[\frac{\mu_r-1}{\mu_r+1}-\left(\frac{R_0}{R_r}\right)^{2np}\right] \tag{9}$$

$$\begin{aligned}K_{B(c)} = &\left[1-\frac{\mu_r-1}{\mu_r+1}\left(\frac{R_s}{R_m}\right)^{2np}\right]\left[\frac{\mu_r-1}{\mu_r+1}\left(\frac{R_r}{R_s}\right)^{2np}-\left(\frac{R_0}{R_s}\right)^{2np}\right]- \\ &\left[\frac{\mu_r-1}{\mu_r+1}\left(\frac{R_m}{R_s}\right)^{2np}-1\right]\left[1-\frac{\mu_r-1}{\mu_r+1}\left(\frac{R_0}{R_r}\right)^{2np}\right]\end{aligned} \tag{10}$$

$$f_{Br}(r) = \left(\frac{R_m}{r}\right)^{np+1}+\left(\frac{r}{R_s}\right)^{np-1}\left(\frac{R_m}{R_s}\right)^{np+1} \tag{11}$$

$$f_{Bc}(r) = \left(\frac{R_m}{r}\right)^{np+1}-\left(\frac{r}{R_s}\right)^{np-1}\left(\frac{R_m}{R_s}\right)^{np+1} \tag{12}$$

where B_r is the PM remanence, and μ_r is the relative permeability. In the same way, the air-gap flux density in region *III* can also be deduced.

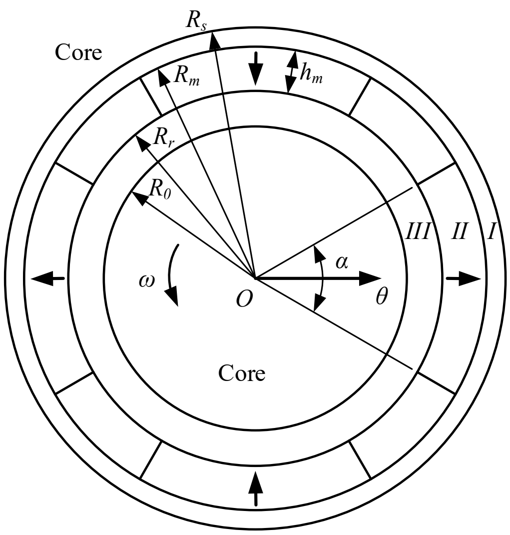

Figure 2. Analytical model of the magnetic field generated by the PMs.

The analytical model of the magnetic field generated by armature windings can be found in [22]. The armature winding current is equivalent to the current sheet at the slot opening of the stator core surface. Solving the Laplace equation of the scalar magnetic potential in the air-gap region, the radial and circumferential components of the air-gap flux density generated by the armature winding also can be derived.

The relative air-gap permeance can be used to derive the air-gap flux density of a slotted model from the air-gap flux density of a slotless model. The complex relative air-gap permeance is obtained through the conformal transformation in [23,24]. The slotted air-gap flux density generated by the PMs B_{ms} and the slotted air-gap flux density generated by the armature windings B_{ws} can be calculated from the slotless air-gap flux density and the relative air-gap permeance.

In order to simplify the analytical calculation of phase back-EMF, the influence of cogging effect on the air-gap flux density is ignored in the calculation of back-EMF. Then, back-EMF of the three-phase winding can be expressed as (13),

$$E_{ph} = 2R_s L_a N_{ph}\omega \sum_{n=1,3,5\cdots}^{\infty} K_B(n) f_{Br}(R_s) K_{pn} K_{dn} \sin(np\omega t) \tag{13}$$

where N_{ph} is the number of turns of each phase, K_{pn} is the winding coil pitch coefficient, K_{dn} is the winding distribution coefficient, and the definition of K_{pn} and K_{dn} is as stated in [25].

For the surface-mounted permanent magnet motor, reluctance torque can be ignored, so electromagnetic torque can be expressed as (14),

$$T_{em} = \frac{E_a i_a + E_b i_b + E_c i_c}{\omega} \tag{14}$$

where E_a, E_b, and E_c are phase back-EMF, i_a, i_b, and i_c are the phase current.

The DC copper loss in the windings, when the temperature is T_w, can be calculated from (15),

$$P_{Cu} = 3I_{ph}R_a[1 + \alpha_T(T_w - T_a)] \tag{15}$$

where I_{ph} is the phase current, R_a is the phase resistance when the temperature is T_a, and α_T is the temperature coefficient of resistance. The AC copper loss induced by skin and proximity effects can be derived as [26]. In fact, due to the low electrical frequency, the AC copper loss of the CRMs in this paper is small enough to be ignored.

The iron loss in the stator cores includes the hysteresis and eddy current loss. The hysteresis and eddy current loss can be calculated from (16) and (17), respectively,

$$P_h = k_h \rho_{sc} V_{sc} {B_{sc,\max}}^{\alpha} f \tag{16}$$

$$P_e = \frac{k_e \rho_{sc} V_{sc}}{2\pi^2} \left\langle \left(\frac{dB_{sc}}{dt} \right)^2 \right\rangle \tag{17}$$

where k_h, k_e, and α are material-dependent constants, based on the empirical loss curves provided by the manufacturer, ρ_{sc} and V_{sc} are the density and volume of the stator core, respectively, f is the electrical frequency, $B_{sc,\max}$ is the maximum magnetic flux density in the stator cores.

The average magnet loss in the magnet segment can be calculated by (18),

$$P_m = \frac{l_a \omega}{2\pi\sigma} \int_0^{2\pi/\omega} \int_{r_1}^{r_2} \int_{\theta_1}^{\theta_2} {J_e}^2 r dr d\theta_r dt \tag{18}$$

where l_a is the active length, σ is the conductivity of magnets, and the definition of J_e is described in detail in [27].

The motor mechanical loss includes the windage and friction losses on the bearings. The windage loss on the rotor can be calculated from (19),

$$P_w = \pi C_f \rho \omega^3 \left(\frac{d_r}{2} \right)^4 l_r \tag{19}$$

where ρ is the fluid density, d_r is the rotor radius, l_r is the rotor length and C_f is the friction coefficient, which can be found in [28]. The friction loss on the bearings can be expressed as (20),

$$P_b = N_b f_b F_r \frac{d_b}{2} \omega \tag{20}$$

where, N_b is the number of bearings, f_b is the friction coefficient of bearings, F_r is the radial force, d_b is the diameter of bearings.

2.3. Optimization Process

For electrically powered underwater vehicles, where CRMs are used to drive the propellers, the torque density and efficiency of the CRMs are expected to be high. Therefore, lighter mass and higher efficiency are set as optimization objectives of CRMs.

The optimization constraints include the output torque T_{out}, the winding current density J_c, and the stator core magnetic density B_{sc}, etc. The motor output torque cannot be compromised. Then, due to heat dissipation, the winding current density is also limited. In addition, the stator core magnetic density cannot exceed the saturation magnetic flux density of the core material.

As a popular multi-objective genetic algorithm, NSGA-II is used to optimize CRMs. The analytical model of CRMs can be used to calculate electromagnetic fields and electromagnetic performance. Optimization variables will be iterated until the optimization constraints are met. A flowchart of the optimization process is shown in Figure 3.

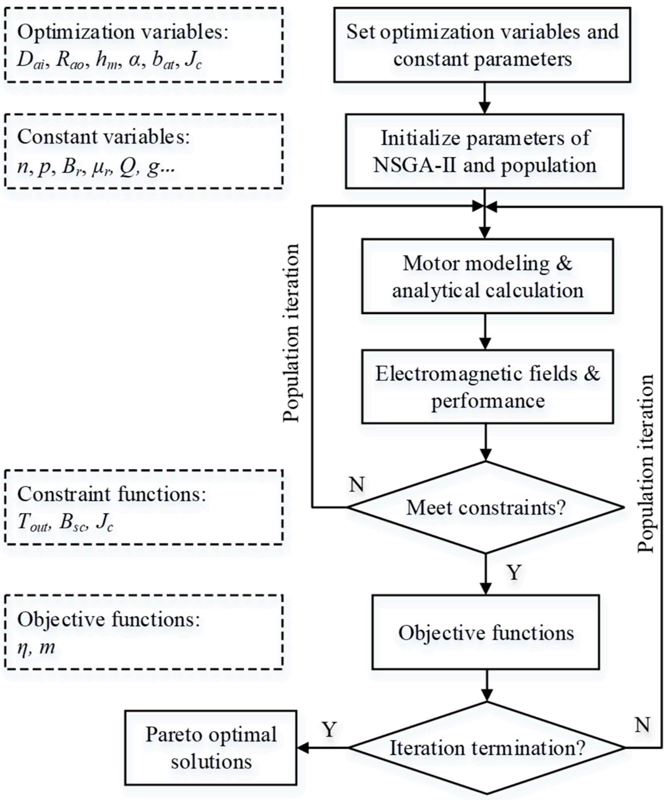

Figure 3. An analytical optimization process flowchart of CRMs.

The CRMs of three different topologies were optimized with the proposed process. For example, the parameters of one motor in DCRMs before and after optimization are shown in Table 1. It can be seen that after optimization, motor efficiency is increased by 1.1% and mass is reduced by 7.3%. In order to verify the analytical calculation, this paper analyzed this optimal solution with the FEA method. The analytical calculation waveform of the air-gap flux density aligns with the FEA results, as illustrated in Figure 4. Although some discrepancies can be observed in the ripples of electromagnetic torque waveform, the FEA and analytical calculation of phase back EMF and electromagnetic torque are in close agreement, as shown in Figure 5.

Table 1. Motor parameters before and after optimization.

Symbol	Quantity	Before Optimization	After Optimization
p	number of poles	10	10
Q	number of slots	60	60
D_{ao}	armature outer diameter	212 mm	220 mm
D_{ai}	armature inner diameter	138 mm	148 mm
l_s	stack length	81 mm	70 mm
b_{at}	armature tooth width	3.68 mm	3.93 mm
h_{ay}	armature yoke thickness	8.6 mm	8.6 mm
g	air-gap width	2.5 mm	2.5 mm
α	pole arc coefficient	0.8	0.83
h_{rc}	rotor core thickness	7.2 mm	7.5 mm
h_m	PM thickness	4.5 mm	5 mm
B_r	remanence	1.13 T	1.13 T
J_c	coil current density	4.5 A/mm^2	4.4 A/mm^2
m	motor mass	14.98	13.89
η	motor efficiency	88.2%	89.3%

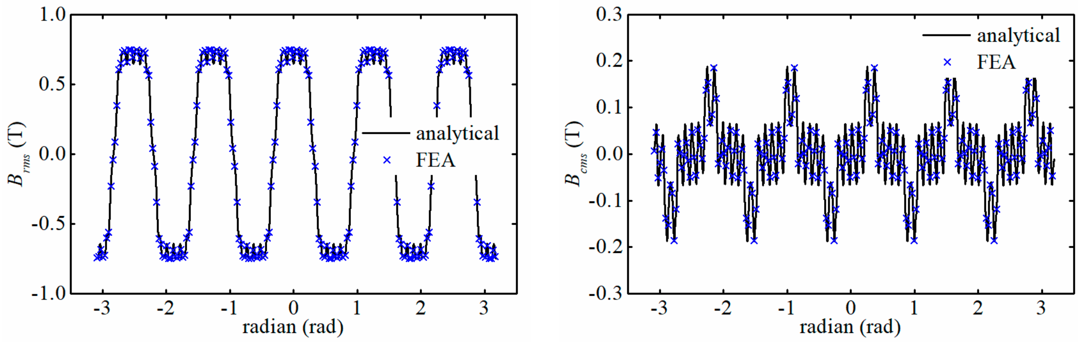

(**a**) (**b**)

Figure 4. (**a**) the radial air-gap flux density distribution waveform, (**b**) the circumferential air-gap flux density distribution waveform, at the center of the air-gap.

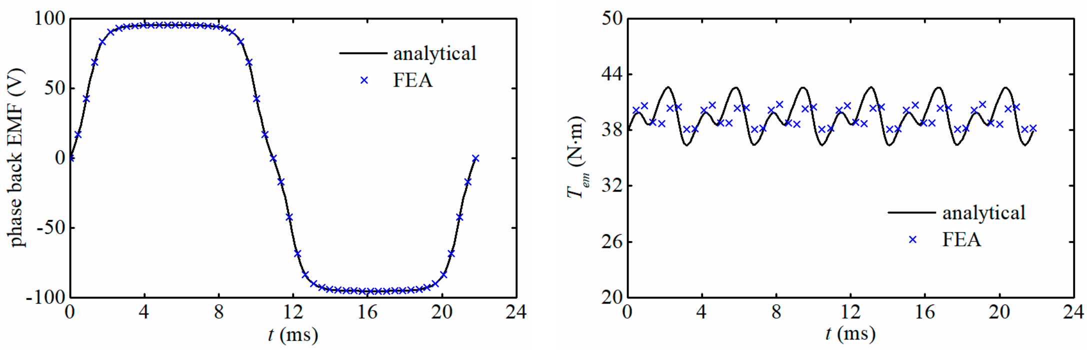

(**a**) (**b**)

Figure 5. (**a**) the phase back EMF waveform, (**b**) the electromagnetic torque waveform.

3. Topologies of CRMs

3.1. DCRMs

DCRMs use two independent motors with opposite rotation directions to drive the two propellers of CRPs. The structure of DCRMs in the tail of underwater vehicles is shown in Figure 6.

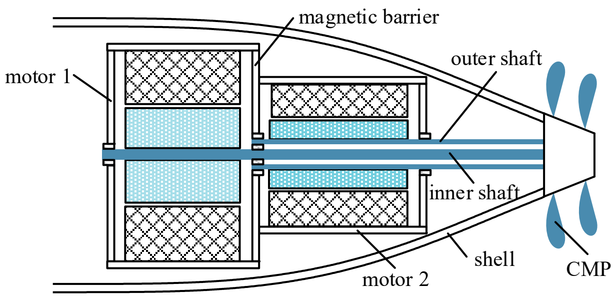

Figure 6. The DCRMs in the tail of underwater vehicles.

Each independent motor of the DCRMs has one single rotor and one single stator, and the output torque and speed of the two motors are equal in magnitude and opposite in direction. In the middle of the two independent motors with opposite rotation directions is the magnetic barrier, which can prevent the magnetic fields of two independent motors on both sides from affecting each other. Analytical calculation of the magnetic field and electromagnetic performance can be used to design and optimize two independent motors of the DCRMs. The parameters of the DCRMs are shown in Table 2. The structure and the magnetic fields of motor 1 in the DCRMs are presented in Figure 7.

Table 2. The parameters of motor 1 and motor 2 in the DCRMs.

Symbol	Quantity	Motor 1	Motor 2
p	number of poles	10	10
Q	number of slots	60	60
D_{ao}	armature outer diameter	253 mm	220 mm
D_{ai}	armature inner diameter	180 mm	148 mm
l_s	stack length	49 mm	70 mm
b_{at}	armature tooth width	4.7 mm	3.93 mm
h_{ay}	armature yoke thickness	10.2 mm	8.6 mm
g	air-gap width	2.5 mm	2.5 mm
α	pole arc coefficient	0.83	0.83
h_{rc}	rotor core thickness	8.5 mm	7.5 mm
h_m	PM thickness	5 mm	5 mm
B_r	remanence	1.13 T	1.13 T
J_c	coil current density	4.4 A/mm^2	4.4 A/mm^2

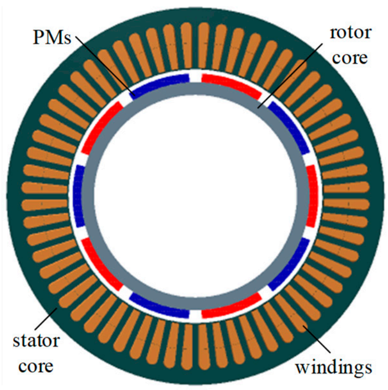

(**a**)

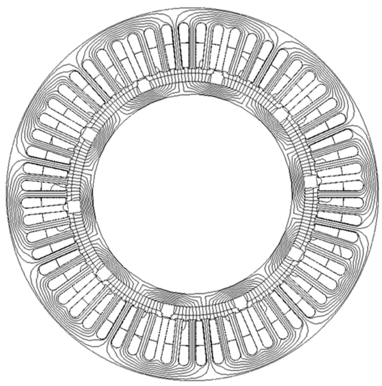

(**b**)

Figure 7. (**a**) The structure of motor 1 in the DCRMs, (**b**) the magnetic fields of motor 1 in the DCRMs.

The efficiency map of the DCRMs calculated by FEA is shown in Figure 8, where the abscissa is the speed of each shaft. The three curves in Figure 8 are the load torque characteristics of three different CRPs. When the output torque is 39 N·m, and the shaft speed is 550 rpm, efficiency of the DCRMs is 89.3%. When the shaft speed is 1500 rpm, efficiency of the DCRMs is 93.5%. When the shaft speed is 3000 rpm, efficiency of the DCRMs is 94%.

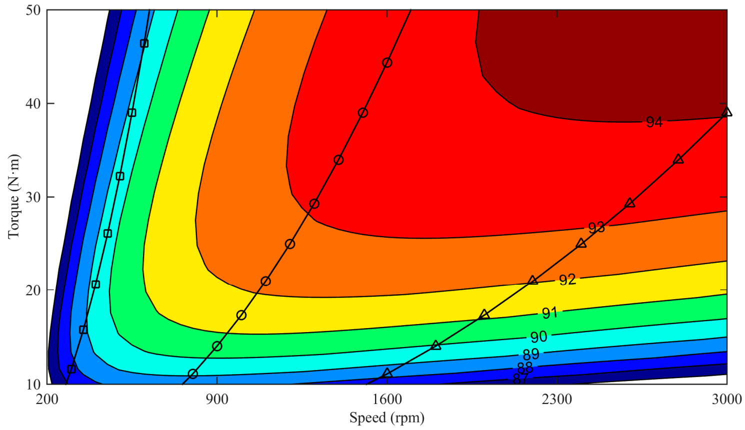

Figure 8. The efficiency map of the DCRMs.

When the output torque is 39 N·m, the shaft speeds are 550 rpm, 1500 rpm, and 3000 rpm, respectively. The loss distribution of the DCRMs is shown in Figure 9. As can be seen from Figure 9, when CRP speed is low, the main loss of the DCRMs is copper loss; this distribution is not conducive to the improvement of the DCRMs' efficiency. As the speed increases, iron loss and mechanical loss gradually occupy a larger proportion.

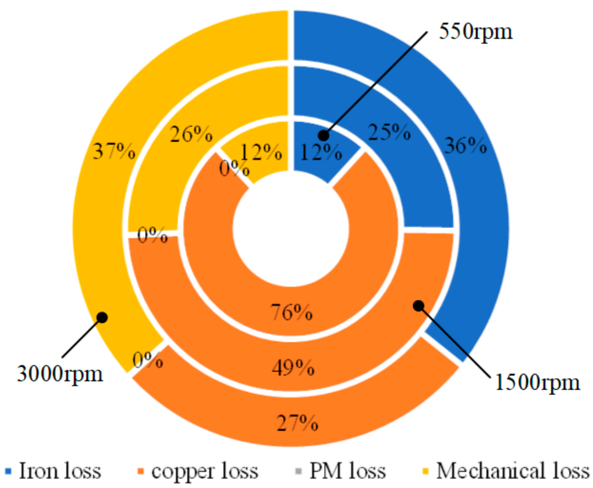

Figure 9. The loss distribution of the DCRMs in different shaft speed.

3.2. DRCRM

A DRCRM has a shared middle stator and two PM rotors rotating in opposite directions to drive the two propellers of the DRP. The structure of a DRCRM is demonstrated in Figure 10. The DRCRM can be seen as one outer rotor motor and another inner rotor motor, and the two stator cores of these two motors are connected back-to-back. The phase sequence of the three-phase armature winding on one side is opposite to the phase sequence of the three-phase armature winding on the other side. Therefore, the rotation direction of the rotors on both sides is opposite. The parameters of the DRCRM are shown in Table 3.

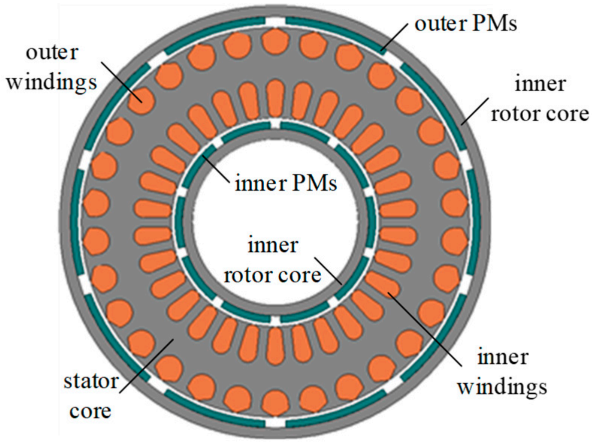

Figure 10. The structure of the DRCRM.

Table 3. The parameters of the DRCRM.

Symbol	Quantity	Value	Symbol	Quantity	Value
p	number of poles per side	5	g	air-gap width per side	2.5 mm
Q	number of slots per side	30	α	pole arc coefficient per side	0.83
D_{ao}	armature outer diameter	277 mm	h_m	outer PM thickness	5 mm
D_{ai}	armature inner diameter	148 mm	h_{rc}	rotor core thickness	13 mm
l_s	stack length	70 mm	B_{ro}	outer PM remanence	0.57 T
b_{at}	armature tooth width	6.9 mm	B_{ri}	inner PM remanence	1.1 T
h_{ay}	armature yoke thickness	17.9 mm	J_c	coil current density	4.4 A/mm^2

Since the relative positions of the PMs on both sides will change at different times, the magnetic fields on both sides of the DRCRM will be periodically in series or in parallel, as shown in Figure 11. It can be seen that when the magnetic fields on both sides are in parallel, the magnetic flux density in the armature yoke will increase.

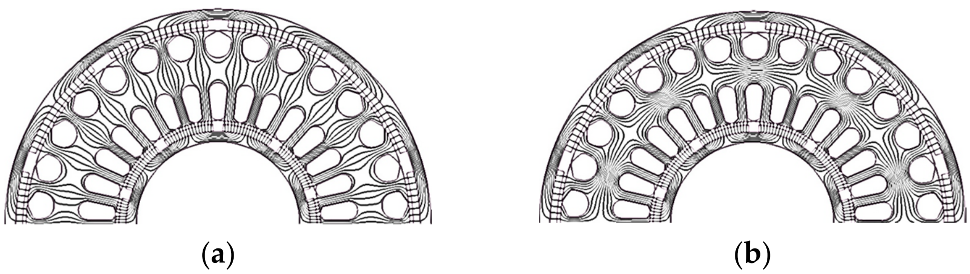

Figure 11. The magnetic fields of the DRCRM on both sides (**a**) in parallel, (**b**) in series.

The armature windings on both sides can also be connected in series or parallel [29], as shown in Figure 12. It can be seen that the end of the windings in series is shorter than that of the windings in parallel. However, the series windings on both sides will cause the crossover points, which may result in underutilization of the armature space. Using the motor optimization process, an inner PM rotor motor and an outer PM rotor motor can be designed and optimized, and the outer diameter of an inner PM rotor motor and the inner diameter of an outer PM rotor motor are equal. In this way, the DRCRM scheme can be obtained.

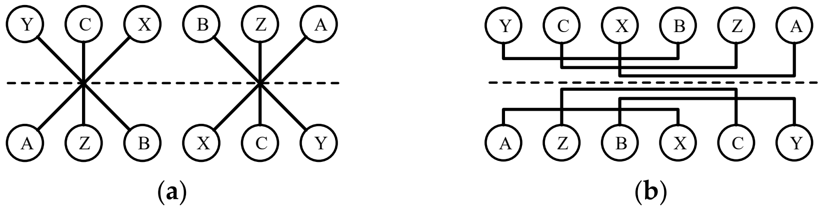

Figure 12. (**a**) End connections with windings on both sides in series, (**b**) end connections with windings on both sides in parallel.

The efficiency map of the DRCRM calculated using the FEA method is shown in Figure 13, where the abscissa is the speed of each shaft. When the output torque is 39 N·m, and the shaft speed is 550 rpm, efficiency of the DRCRM is 88.3%. When the shaft speed is 1500 rpm, efficiency of the DCRM is 93.1%. When the shaft speed is 3000 rpm, efficiency of the DCRM is 93.8%.

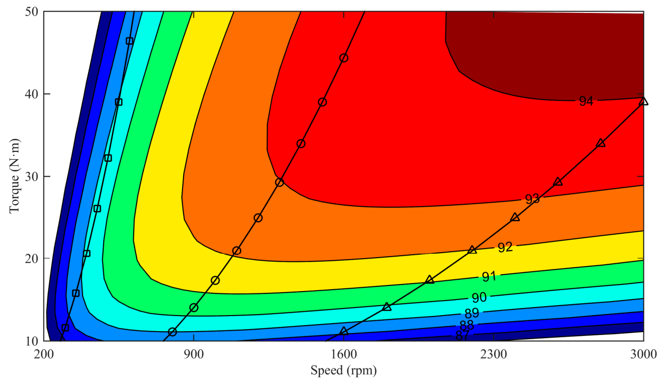

Figure 13. The efficiency map of the DRCRM.

When the output torque is 39 N·m, the shaft speeds are 550 rpm, 1500 rpm, and 3000 rpm, respectively; the loss distribution of the DRCRM is shown in Figure 14. It can be seen that compared with the DCRMs, the efficiency and loss of the DRCRM have no advantages. This is because the size of the magnetic circuits on the inner and outer sides of the DRCRM is quite different. Therefore, it is difficult to optimize the structure on both the inside and outside at the same time.

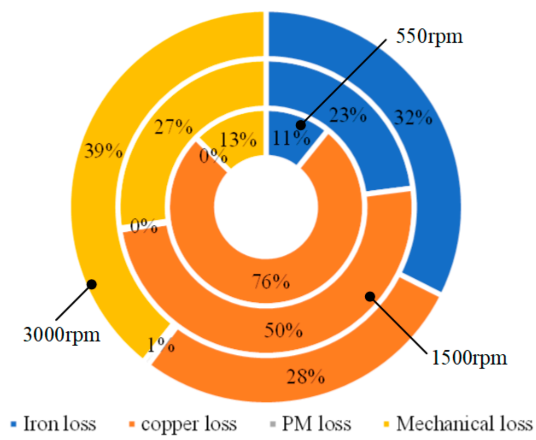

Figure 14. The loss distribution of the DRCRM.

3.3. ARCRM

An ARCRM from the tail of an underwater vehicle is shown in Figure 15. This solution for CRMs utilizes the reaction force between the PM rotor and the armature to drive them to rotate in opposite directions. The armature is in the inner rotor, and the PMs are in the outer rotor. The armature is supported on the motor housing by the inner rotor hub, inner shaft, and bearings. The PM rotor is supported on the motor housing by the outer rotor end cap, outer shaft, and bearings. In this way, the ARCRM can provide two output torque of opposite directions and equal magnitude, so that the inner and outer output shafts of the ARCRM, respectively, drive two single propellers of the CRP to rotate in the opposite direction. The main parameters of the ARCRM are shown in Table 4. The structure and magnetic fields of the ARCRM are presented in Figure 16.

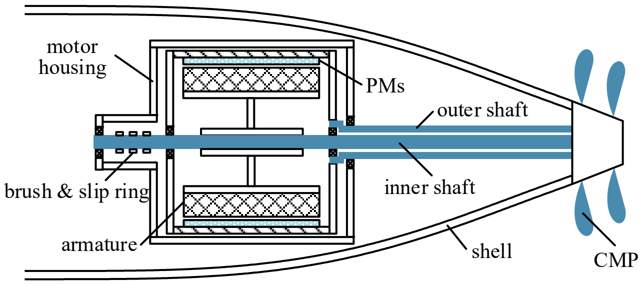

Figure 15. The ARCRM in the tail of underwater vehicles.

Table 4. The parameters of the ARCRM.

Symbol	Quantity	Value	Symbol	Quantity	Value
p	number of poles	12	g	air-gap width	2.5 mm
Q	number of slots	72	α	pole arc coefficient	0.8
D_{ao}	armature outer diameter	230 mm	h_m	PM thickness	5 mm
l_s	stack length	58 mm	h_{rc}	rotor core thickness	10 mm
b_{at}	armature tooth width	4.2 mm	B_r	remanence	1.13 T
h_{ay}	armature yoke thickness	16.2 mm	J_c	coil current density	4.4 A/mm^2

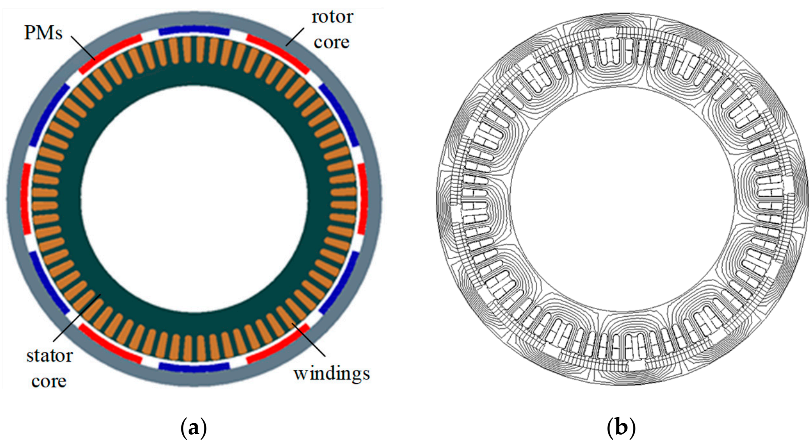

Figure 16. (**a**) The structure of the ARCRM, (**b**) the magnetic fields of the ARCRM.

In order to rotate both the PM rotor and the armature, additional mechanical structures are also required, such as an outer rotor end cap and bearings. Essentially, these mechanical structures are "transmissions" that amplify the relative speed between the PMs and the armature to twice the rated speed of a single propeller. The relative speed between the PMs and the armature is the sum of the inner and outer rotor speed. However, the armature windings also rotate, so power needs to be supplied to the armature windings through brushes and slip rings.

The motor efficiency map calculated using the FEA method is shown in Figure 17, where the abscissa is the speed of each shaft. When the output torque is 39 N·m, and the shaft speed is 550 rpm, efficiency of the ARCRM is 93.7%. When the shaft speed is 1500 rpm, efficiency of the ARCRM is 94.1%. When the shaft speed is 3000 rpm, efficiency of the ARCRM is 92.6%. A further increase of the speed is not conducive to the improvement of efficiency.

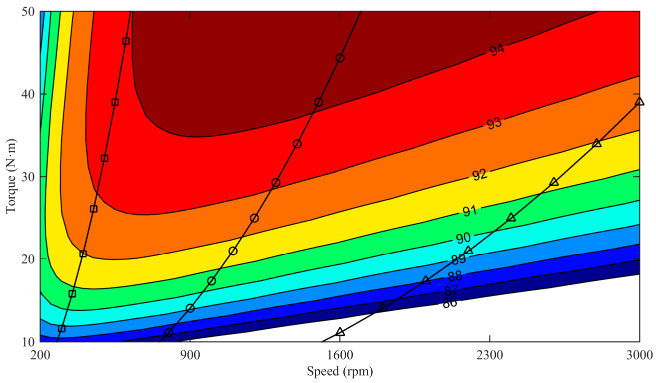

Figure 17. The efficiency map of the ARCRM.

When the output torque is 39 N·m, the shaft speeds are 550 rpm, 1500 rpm, and 3000 rpm, respectively. The loss distribution of the ARCRM is shown in Figure 18. Since the relative speed of the ARCRM is amplified to twice the rated speed of the single propeller, although the CRP speed is low, the loss of the ARCRM is uniformly distributed, which will benefit efficiency improvement. When the CRP speed is low, the loss of the ARCRM is uniformly distributed, which will benefit efficiency improvement. However, when the speed is too high, iron loss will become the main loss. This distribution is not conducive to improving efficiency.

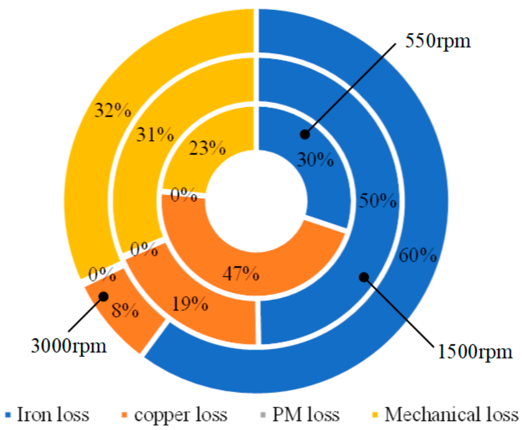

Figure 18. The loss distribution of the ARCRM.

4. Comparison of Topologies

In this paper, the topologies of DCRMs, the DRCRM, and the ARCRM are presented to drive the CRPs of underwater vehicles. The following will compare these three topologies for CRMs from the perspectives of structure, weight, size, loss, and efficiency.

4.1. Structure

DCRMs: the structure is simple and easy to implement, and no brushes and slip rings are required. Therefore, reliability and robustness are higher. However, the relative speed between the PMs and the armature is only half of that of the ARCRM, resulting in a decrease in electrical frequency. On the one hand, iron loss in the stator core is reduced; however, the properties of the stator core material cannot be fully utilized. Because the magnetic fields of the two motors are independent of each other, both rotors can be assigned to different speeds and torque.

DRCRM: the magnetic fields on both sides will be periodically in parallel and in series. However, for the DRCRM, the speed and load torque of the two contra-rotating rotors may be different, especially during the starting of the motor. The speed difference will distort the magnetic field. In addition, when the torque of the two rotors is different, the current of armature windings on both sides will also be different, which will also cause an imbalance of the rotors on both sides. Since the DRCRM is sensitive to speed or load torque, the robustness of the DRCRM is still poor, and further research is needed on the control strategies. In order to balance the magnetic fields on both sides, both rotors have to be assigned the same speed and torque.

ARCRM: due to the rotation of the armature, the relative speed between the PMs and the armature doubles the rated speed of a single propeller of the CRP, thus contributing to increased power density. However, additional mechanical structures are required to rotate both the PM rotor and the armature, and brushes and slip rings are necessary to power the rotating armature winding. The output torque of the two rotors is always equal due to the reactive force, but the two output ports can be assigned to different speeds.

4.2. Weight and Size

A mass and size comparison of three CRMs with different magnetic circuit topologies is shown in Table 5. It should be noted that the weight and size of the three CRMs only include the stator and rotor cores, PMs, and winding copper wire, excluding the motor housing and additional mechanical structures. The speeds in Table 5 are the speeds between the armature and PMs. For convenient comparison, the winding current density and the core magnetic density are designed to be the same.

Table 5. Weight and size comparison of three CRMs.

	DCRMs	DRCRM	ARCRM		DCRMs	DRCRM	ARCRM
armature core (kg)	13	13.94	6.66	stack length (mm)	119	70	58
armature windings (kg)	9.82	9.65	2.93	speed (rpm)	550	550	550×2
PMs (kg)	1.9	2.53	1.33	torque (N·m)	39	39	39
rotor core (kg)	3.07	5.62	3.67	power (kW)	4.5	4.5	4.5
total mass (kg)	27.79	31.74	14.59	power factor	0.927	0.898	0.937
outer diameter (mm)	253	308	265	efficiency	89.3%	88.3%	93.7%

The ARCRM utilizes the reaction force between the armature and the PM, and only one set of the magnetic circuit is required, so the mass and size of the ARCRM are minimal. The DRCRM has a magnetic circuit topology with inner and outer double rotors and a middle stator. It is difficult to achieve an optimal design of the inner and outer magnetic circuits, simultaneously. Therefore, the DRCRM has the largest mass and size.

4.3. Loss and Efficiency

When the shaft torque is 39 N m, the losses of three CRMs with different magnetic circuit topologies at different speeds are shown in Figure 19.

As seen from (a), iron loss of the ARCRM is the largest, much higher than that of DCRMs and the DRCRM. This is because the relative speed between the PM and armature of the ARCRM is twice that of DCRMs and the DRCRM, and the electrical frequency is higher. Iron loss of the DRCRM is slightly smaller than that of DCRMs because the magnetic circuits on both sides of the DRCRM are periodically connected in series and in parallel; when the magnetic circuits are connected in series, the losses in the armature yoke are reduced.

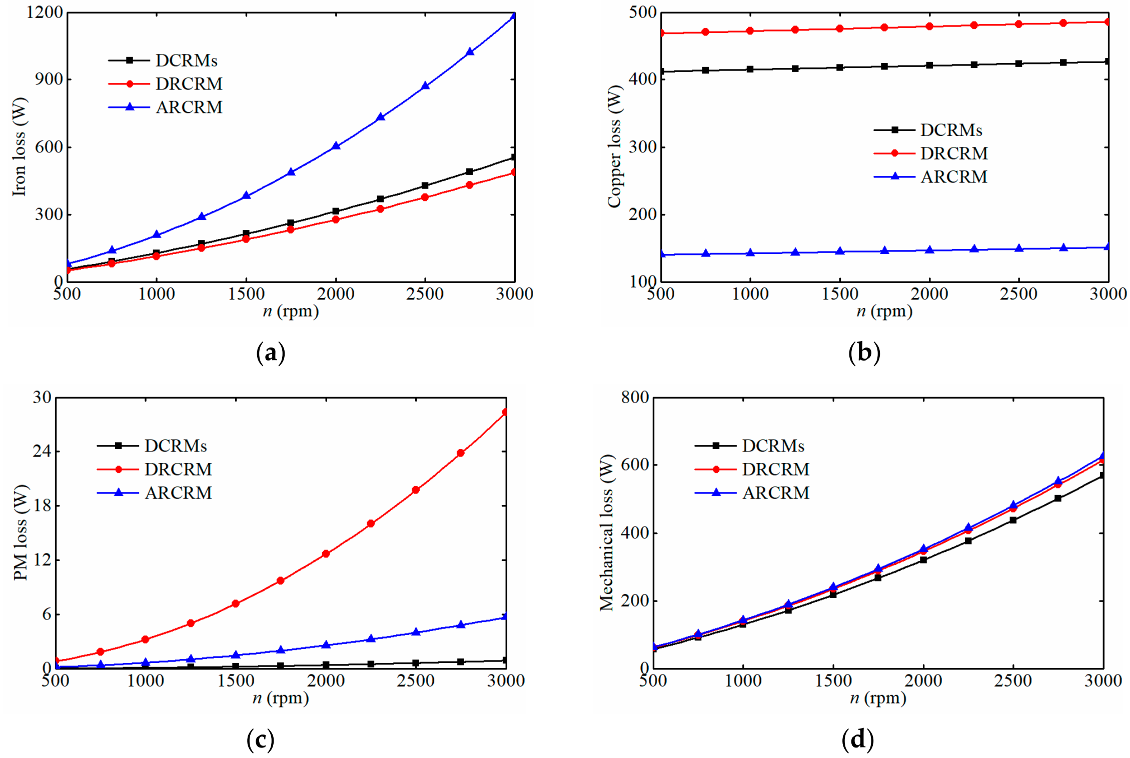

Figure 19. The losses of three CRMs with different magnetic circuit topologies at different speeds. (**a**) iron loss, (**b**) copper loss, (**c**) PM loss, (**d**) mechanical loss.

As seen from (b), copper loss of the ARCRM is much smaller than that of DCRMs and the DRCRM. This is because the ARCRM uses the reaction force to output torque, so only one set of the magnetic circuit is needed, and the amount of copper wire and copper loss is smaller. In addition, since it is difficult to optimize the inside and outside magnetic circuits of the DRCRM at the same time, the copper loss of the outer magnetic circuit is larger, and the copper loss of the DRCRM will be slightly larger than that of DCRMs.

As seen from (c), PM loss of the DRCRM is the largest, much larger than that of DCRMs and the ARCRM. This is because the PM remanence of the DRCRM outer magnetic circuit is small, but the volume and weight are large, so the eddy current loss in the outer PM is also large.

The efficiencies of three CRMs with different magnetic circuit topologies at different speeds are shown in Figure 20. When the speed is low, the efficiency of the ARCRM has obvious advantages. However, when the speed exceeds 2000 rpm, the efficiency of the ARCRM gradually lags. Therefore, the ARCRM is suitable for CRPs with low-rated speeds. It can also be seen that DCRMs are consistently slightly more efficient than DRCRMs, but the difference is small.

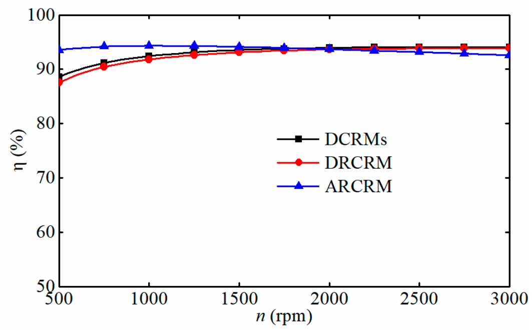

Figure 20. The efficiencies of three CRMs with different magnetic circuit topologies at different speeds.

5. Experiment and Validation

An ARCRM prototype has been designed and fabricated, and the bench test of the ARCRM prototype is demonstrated in Figure 21. The stator phase currents are continuously monitored using current sensors and an oscilloscope. During operation, real-time temperature measurements are taken at the midpoint of the end winding using infrared thermometers with an accuracy of 1%. The speed and torque sensor boasts a remarkable accuracy of ±0.1%. The ambient temperature during the test is maintained at 20 °C. The motor prototype is powered by a DC power supply through the controller, with the DC voltage set to 210 V. When the ARCRM prototype was driven by the load motor at 2 × 550 rpm, the power consumed by the ARCRM prototype was taken as no-load iron and mechanical losses. The measured copper loss can be obtained from the measured phase current and the measured phase resistance at the operating temperature. Moreover, from the above analysis and calculation, it can be seen that the PM loss of the ARCRM prototype can be negligible. When the rotating speed is 550 × 2 rpm, and the output torque is 39 Nm, the measured losses of the ARCRM prototype are shown in Table 6.

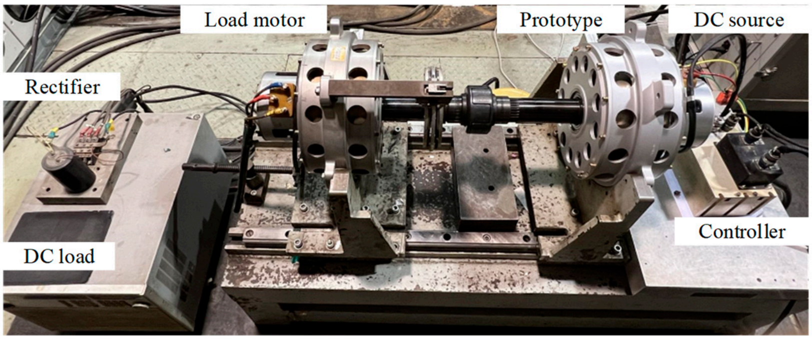

Figure 21. The prototype of the ARCRM.

Table 6. The measured losses of the ARCRM prototype.

Calculated		Measured	
Copper loss	140.5 W	Copper loss	140.4 W
Iron loss	91.1 W	No-load iron loss, mechanical loss	167.3 W
Mechanical loss	70.5 W		

Based on the motor's output torque, speed, and losses, it can be calculated that the motor's efficiency is 93.7%. Under the rated load, the mechanical output characteristics of the ARCRM prototype are shown in Table 7. The output torque of the inner shaft is 0.4 Nm less than that of the outer shaft because the mechanical loss of the inner shaft is larger due to the friction between the brushes and slip rings. The rotational speed of the inner shaft is 1.4% lower than that of the outer rotor, due to the larger friction and larger inertia of the inner shaft.

Table 7. The mechanical output characteristics of the ARCRM prototype.

	Output Torque	Rotational Speed
Inner shaft	39 Nm	546 rpm
Outer shaft	39.4 Nm	554 rpm

In order for the motor prototype to operate reliably during the test, the temperature at the winding end was monitored. The three-dimensional lumped circuit model was used to calculate the transient thermal characteristics of the ARCRM prototype, and this thermal model was solved using ANSYS Motor-CAD software. When the ambient temperature was 20 °C, the prototype worked for 7 h under the rated load, and the calculated and measured winding temperature of the ARCRM prototype is shown in Figure 22. The maximum temperature measured at the winding end was 109 °C. The insulation grade of the winding copper wire was class H. Therefore, the temperature of the armature windings was always in the safe area, and the prototype remained safe throughout the testing process.

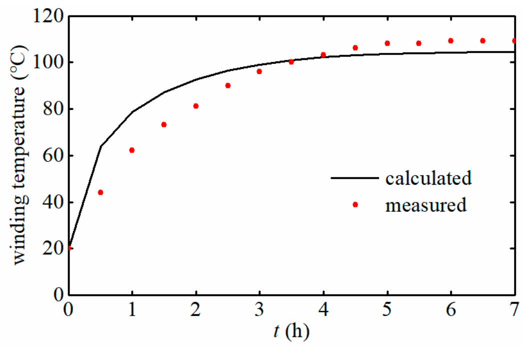

Figure 22. Winding temperature during the bench test.

But for the ARCRM, the reliability of brushes and slip rings is the focus of this motor research. Therefore, we tested the ARCRM prototype for 800 cycles, and the test cycle number even exceeded the maximum cycle number allowed by the battery. The slip ring before and after the 7 × 800 h test is shown in Figure 23. That is to say, the brushes and slip ring still can normally work after 7 × 800 h of operation, which means that the brushes and slip rings are not the factors that limit motor life.

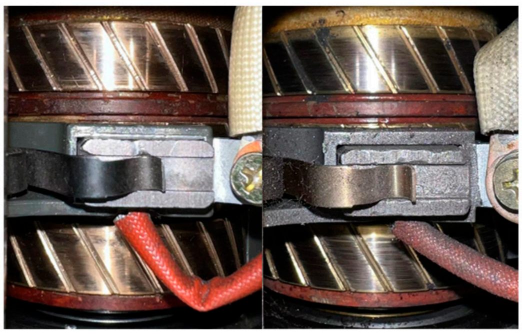

Figure 23. The slip ring of the ARCRM prototype (**a**) before the test, (**b**) after the test.

6. Conclusions

This paper presented the analytical optimization process and the comparison of DCRMs, DRCRMs, and ARCRMs to drive the CRPs of underwater vehicles. The efficiency and power density of DCRMs are lower due to the low speed and high torque. The speed and torque of the double rotor of the DRCRM should be equal to avoid distortion of the magnetic fields on both sides. Such speed and torque requirements are difficult to achieve under the prior art of the control strategy. Therefore, at present, the DRCRM may not be suitable for driving CRPs of underwater vehicles. The ARCRM has high efficiency and power density because the relative speed between the PMs and the armature is amplified to twice the rated speed of a single propeller of the CPRs. The experimental testing of the ARCRM prototype shows that the analytical design and optimization process are credible, and the ARCRM can operate reliably from the perspective of temperature and slip rings.

Author Contributions: B.C. is the main author of this manuscript; S.P. made suggestions for this work; H.O. contributed to the development of the prototype; Z.H. worked on the experiment of the prototype; Z.M. reviewed and edited the draft. All authors have read and agreed to the published version of the manuscript.

Funding: This work was supported by the National Natural Science Foundation of China (Grant No. 51879220).

Institutional Review Board Statement: Not applicable.

Informed Consent Statement: Not applicable.

Data Availability Statement: Not applicable.

Conflicts of Interest: The authors declare no conflict of interest.

References

1. Yang, X.; Tang, S.; Yuan, X.; Wang, X.; Zhu, J. Modeling and the Control Strategy of the Coaxial Contra-Rotating Propeller System. In Proceedings of the International Conference on Autonomous Unmanned Systems, Changsha, China, 24–26 September 2021; pp. 2139–2148.
2. Huang, Y.; Dong, X.; Yang, C.; Li, W.; Noblesse, F. Design of wake-adapted contra-rotating propellers for high-speed underwater vehicles. *Appl. Ocean Res.* **2019**, *91*, 101880. [CrossRef]
3. Huang, Y.; Yang, J.; Yang, C. Numerical prediction of the effective wake profiles of a high-speed underwater vehicle with contra-rotating propellers. *Appl. Ocean Res.* **2019**, *84*, 242–249. [CrossRef]
4. Lyu, C.; Lu, D.; Xiong, C.; Hu, R.; Jin, Y.; Wang, J.; Zeng, Z.; Lian, L. Toward a gliding hybrid aerial underwater vehicle: Design, fabrication, and experiments. *J. Field Robot.* **2022**, *39*, 543–556. [CrossRef]
5. Liu, G.; Qiu, G.; Shi, J.; Zhang, F. Study on counter-rotating dual-rotor permanent magnet motor for underwater vehicle propulsion. *IEEE Trans. Appl. Supercond.* **2018**, *28*, 1–5. [CrossRef]
6. Ranlöf, M.; Lundin, U. Finite element analysis of a permanent magnet machine with two contra-rotating rotors. *Electr. Power Compon. Syst.* **2009**, *37*, 1334–1347. [CrossRef]
7. Ranlof, M.; Connor, G.; Lundin, U. Simulation of a radial flux permanent magnet generator with two contra-rotating rotors. In Proceedings of the 2008 18th International Conference on Electrical Machines, Vilamoura, Portugal, 6–9 September 2008; pp. 1–6.
8. Caricchi, F.; Crescimbini, F.; Santini, E. Basic principle and design criteria of axial-flux PM machines having counterrotating rotors. *IEEE Trans. Ind. Appl.* **1995**, *31*, 1062–1068. [CrossRef]
9. Zhang, F.; Gao, Y.; Chen, J. Design and analysis of a novel wind-power permanent magnet generator with Opposite-rotation dual rotors. In Proceedings of the 2010 International Conference on Electrical Machines and Systems, Incheon, Republic of Korea, 10–13 October 2010; pp. 1681–1686.
10. Zhang, F.; Liu, G.; Shen, Y.; Wang, F. Characteristic study on a novel PMSM with opposite-rotation dual rotors. In Proceedings of the 2007 International Conference on Electrical Machines and Systems (ICEMS), Seoul, Republic of Korea, 8–11 October 2007; pp. 805–809.
11. Chen, J.; Zhang, F.; Zhang, W. No-load torque ripple analysis of a novel permanent magnet synchronous motor with anti-rotation dual rotors using finite element method. In Proceedings of the 2011 International Conference on Electrical Machines and Systems, Beijing, China, 20–23 August 2011; pp. 1–5.
12. Zhang, F.; Chen, J.; Liu, G. Research on Counter-rotating Dual Rotors Permanent-magnet Machine for underwater vehicle. In Proceedings of the 2014 IEEE Conference and Expo Transportation Electrification Asia-Pacific (ITEC Asia-Pacific), Beijing, China, 31 August–3 September 2014; pp. 1–7.
13. Zhong, Y.; Huang, S.; Luo, D.; He, R. Speed synchronism of permanent magnet synchronous motor with dual contra-rotating rotors under load variation. *IET Power Electron.* **2017**, *10*, 1479–1486. [CrossRef]
14. Cheng, S.; Luo, D.; Huang, S.; Chen, Z.; Huang, K. Control strategy for permanent magnet synchronous motor with contra-rotating rotors under unbalanced loads condition. *IET Electr. Power Appl.* **2015**, *9*, 71–79. [CrossRef]
15. Zhong, Y.; Huang, S.; Luo, D. Stabilization and speed control of a permanent magnet synchronous motor with dual-rotating rotors. *Energies* **2018**, *11*, 2786. [CrossRef]
16. Zhong, Y.; Huang, S.; Luo, D.; Wu, X. Characteristics of an axial-flux permanent magnet synchronous machine with contra-rotating rotors under unbalanced load condition from 3-D finite element analysis. *CES Trans. Electr. Mach. Syst.* **2018**, *2*, 220–225. [CrossRef]
17. Hassannia, A. Self-compensation of torque reaction in an induction contra-rotating propulsion motor. *IET Electr. Power Appl.* **2022**, *16*, 941–951. [CrossRef]
18. Chen, H.; El-Refaie, A.M.; Zuo, Y.; Cai, S.; Xie, S.; Lee, C.H. Evaluation of a Contra-Rotating Flux-Modulated Machine Featured with Dual Flux-Modulation for Wind Power Generation. *IEEE Trans. Ind. Electron.* **2021**, *69*, 8770–8781. [CrossRef]
19. Mirnikjoo, S.A.; Asadi, F.; Abbaszadeh, K.; Abdollahi, S.E. Effect of rotor topology on the performance of counter-rotating double-sided flux switching permanent magnet generator. *IEEE Trans. Energy Convers.* **2021**, *37*, 65–74. [CrossRef]
20. Baek, D.; Yoon, H.; Jung, J.; Kim, K.; Paik, B. Effects of the advance ratio on the evolution of a propeller wake. *Comput. Fluids* **2015**, *118*, 32–43. [CrossRef]
21. Kinaci, O.K.; Bayezit, I.; Reyhanoglu, M. A practical feedforward speed control system for autonomous underwater vehicles. *Ocean Eng.* **2020**, *218*, 108214. [CrossRef]

22. Zhu, Z.Q.; Howe, D. Instantaneous magnetic field distribution in brushless permanent magnet DC motors. II. Armature-reaction field. *IEEE Trans. Magn.* **1993**, *29*, 136–142. [CrossRef]
23. Zhu, Z.Q.; Howe, D. Instantaneous magnetic field distribution in brushless permanent magnet DC motors. III. Effect of stator slotting. *IEEE Trans. Magn.* **1993**, *29*, 143–151. [CrossRef]
24. Zarko, D.; Ban, D.; Lipo, T.A. Analytical calculation of magnetic field distribution in the slotted air gap of a surface permanent-magnet motor using complex relative air-gap permeance. *IEEE Trans. Magn.* **2006**, *42*, 1828–1837. [CrossRef]
25. Bianchi, N.; Prè, M.D. Use of the star of slots in designing fractional-slot single-layer synchronous motors. *IEE Proc. Electr. Power Appl.* **2006**, *153*, 459–466. [CrossRef]
26. Mellor, P.; Wrobel, R.; Simpson, N. AC losses in high frequency electrical machine windings formed from large section conductors. In Proceedings of the 2014 IEEE Energy Conversion Congress and Exposition (ECCE), Pittsburgh, PA, USA, 14–18 September 2014; pp. 5563–5570.
27. Wu, L.J.; Zhu, Z.Q.; Staton, D.; Popescu, M.; Hawkins, D. Analytical model for predicting magnet loss of surface-mounted permanent magnet machines accounting for slotting effect and load. *IEEE Trans. Magn.* **2011**, *48*, 107–117. [CrossRef]
28. Burnand, G.; Araujo, D.M.; Koechli, C.; Perriard, Y. Validation by measurements of a windage losses model for very-high-speed machines. In Proceedings of the 2017 20th International Conference on Electrical Machines and Systems (ICEMS), Sydney, NSW, Australia, 11–14 August 2017; pp. 1–4.
29. Cheng, B.; Pan, G.; Mao, Z. An Axial Flux Double-Rotor Counter-Rotating Permanent Magnet Machine for Underwater Vehicles. In Proceedings of the 2019 IEEE 8th International Conference on Advanced Power System Automation and Protection (APAP), Xi'an, China, 21–24 October 2019; pp. 1304–1308.